

# DISPATCH: A Numerical Simulation Framework for the Exa-scale Era. I. Fundamentals

Åke Nordlund,<sup>1</sup><sup>★</sup> Jon P. Ramsey,<sup>1</sup><sup>†</sup> Andrius Popovas<sup>1</sup> and Michael Küffmeier,<sup>1</sup>

<sup>1</sup>Center for Star and Planet Formation, the Niels Bohr Institute and the Natural History Museum of Denmark, University of Copenhagen, Øster Voldgade 5-7, DK-1350 Copenhagen, Denmark

Accepted XXX. Received YYY; in original form ZZZ

## ABSTRACT

We introduce a high-performance simulation framework that permits the semi-independent, task-based solution of sets of partial differential equations, typically manifesting as updates to a collection of “patches” in space-time. A hybrid MPI/OpenMP execution model is adopted, where work tasks are controlled by a rank-local “dispatcher” which selects, from a set of tasks generally much larger than the number of physical cores (or hardware threads), tasks that are ready for updating. The definition of a task can vary, for example, with some solving the equations of ideal magnetohydrodynamics (MHD), others non-ideal MHD, radiative transfer, or particle motion, and yet others applying particle-in-cell (PIC) methods. Tasks do not have to be grid-based, while tasks that are may use either Cartesian or orthogonal curvilinear meshes. Patches may be stationary or moving. Mesh refinement can be static or dynamic. A feature of decisive importance for the overall performance of the framework is that time steps are determined and applied locally; this allows potentially large reductions in the total number of updates required in cases when the signal speed varies greatly across the computational domain, and therefore a corresponding reduction in computing time. Another important feature is a load balancing algorithm that operates “locally” and aims to simultaneously minimize load and communication imbalance. The framework generally relies on already existing solvers, whose performance is augmented when run under the framework, due to more efficient cache usage, vectorization, local time stepping, plus near-linear and, in principle, unlimited OpenMP and MPI scaling.

**Key words:** methods: numerical – magnetohydrodynamics (MHD) – stars: formation – planets and satellites: formation – radiative transfer

## 1 INTRODUCTION

Numerical simulations of astrophysical phenomena are indispensable in furthering our understanding of the Universe. A particularly successful example is the many efforts to model the equations of magnetohydrodynamics (MHD) as applied to the varied topics of cosmology, galaxy evolution, star formation, stellar evolution, solar and stellar activity, and planet formation. As the available computer power has increased over time, so too has the fidelity and complexity of astrophysical fluid simulations; more precisely, one could say these simulations have consistently been at the limit of what is computationally possible. The algorithms and techniques used to exploit the available resources have also increased in ingenuity and complexity over the years; from block-based adaptive mesh refinement (AMR; Berger

& Olinger 1984; Berger & Colella 1989) to space-filling curves (e.g. Peano-Hilbert) to non-blocking distributed communication (e.g. Message Passing Interface version 3; MPI). The next evolution in high performance computing (HPC), “exa-scale”<sup>1</sup>, is approaching and, as currently available tools are quickly reaching their limits (see, e.g., Dubey et al. 2014), new paradigms and techniques must be developed to fully exploit the upcoming generation of supercomputers.

There are many astrophysical fluid simulation codes currently available within the scientific community. The most commonly used techniques include single grids (e.g. ZEUS; Stone & Norman 1992; Clarke 1996, FARGO; Maset 2000, PLUTO; Mignone et al. 2007, ATHENA; Stone et al. 2008, PENCIL; Brandenburg & Dobler 2002, STAGGER; Nordlund et al. 1994; Kritsuk et al. 2011, BIFROST;

<sup>★</sup> E-mail: aake@nbi.ku.dk (ÅN)

<sup>†</sup> jramsey@nbi.ku.dk (JPR)

<sup>1</sup> Exa-scale computing is defined as the use of computer systems capable of  $10^{18}$  floating point operations per second.

Gudiksen et al. 2011), adaptively refined grids (e.g. ART; Kravtsov et al. 1997, NIRVANA; Ziegler 1998, ORION; Klein 1999, FLASH; Fryxell et al. 2000, RAMSES; Teyssier 2002; Fromang et al. 2006, AstroBEAR; Cunningham et al. 2009, CASTRO; Almgren et al. 2010, CRASH; van der Holst et al. 2011, AZEuS; Ramsey et al. 2012, ENZO; Bryan et al. 2014, AMRVAC; Porth et al. 2014) and smoothed particle hydrodynamics (e.g. GADGET; Springel 2005, PHANTOM; Lodato & Price 2010). More recently, moving mesh and meshless methods have begun to emerge (e.g. AREPO; Springel 2010, TESS; Duffell & MacFadyen 2011, GIZMO; Hopkins 2015). The range of physics available from one code to the next is very broad, and includes (but is not limited to) radiative transport, heating and cooling, non-ideal MHD, cosmological expansion, special and general relativity, multiple fluids, conduction, and self-gravity. There also exists a growing collection of frameworks which are solver- and physics-agnostic, but instead manage the parallelism, communication, scheduling, input/output and even resolution of a simulation (e.g. BoxLib<sup>2</sup>, Charm++, Kale et al. 2008, Chombo; Adams et al. 2015, Overture; Brown et al. 1997, Uintah; Berzins et al. 2010, PATCHWORK; Shiokawa et al. 2017). Indeed, a few of these frameworks already couple to some of the aforementioned simulation codes (e.g. PLUTO+CHOMBO, BoxLib+CASTRO). Nearly all of the codes and frameworks mentioned above have fundamental weaknesses which limit their applicability and reliability (see, e.g., the discussion in Dubey et al. 2014; Hopkins 2015). In the context of supercomputer simulations, a particularly relevant example is that traditional grid-based codes must advance using time steps that obey the worst possible condition throughout the simulation volume, advancing at some fraction of a time step  $\Delta t = \min(\Delta x/v_{\text{signal}})$ . The time step may be determined locally, but it is applied globally. A global time step which is controlled by a tiny fraction of the computational volume is problematic, and this problem will unavoidably become exasperated as supercomputers grow larger and the physical complexity of models correspondingly increases.

Parallelism in both specific codes and frameworks is almost always implemented using (distributed-memory) MPI, shared-memory thread-based parallelism (e.g. OpenMP, pthreads), or a combination of the two. Although MPI has its limitations (e.g. no fault tolerance), and new approaches are beginning to emerge (e.g. partitioned global address space; PGAS), it is the de facto standard for distributed-computing and will likely remain so leading up to the exa-scale era. Therefore, efficient and clever use of MPI is necessary to ensure performance and scaling do not degrade as we attempt to use the ever-growing resources enabled by ever-larger supercomputers (e.g. Mendygral et al. 2017). An important aspect of this is load balancing, whereby a simulation redistributes the work dynamically in an attempt to maintain an even workload across resources.

Herein, we put forward and explore novel techniques that not only enable better utilization and scaling for the forthcoming exa-scale era, but immediately offers distinct advantages for existing tools. Key to this, among other features, are: The concept of locally determined time steps,

which, in realistic situations, can lead to dramatic savings of computing time. Second, the closely related concept of task-based execution, where each task depends on only a finite number of “neighbouring” tasks. These tasks are often, but not necessarily, geometrically close. For example, neighbouring *patches* need to supply guard zone values of density, momentum, etc., but neighbouring *tasks* can encompass radiative transfer tasks with rays passing through the patch, or particle-based tasks, where particles travel through and interact with gas in a grid-based task. The “neighbour” concept can thus also be described as a “dependency” concept. By relying on this concept, we can ensure that MPI processes only need to communicate with a finite number of other MPI processes and, thus, we can to a large (and often complete) extent avoid any use of MPI global communications. In this regard, the neighbour concept provides the potential for essentially unlimited MPI scalability. The avoidance of global operations and the neighbour concept also extends to intra-node OpenMP parallelism: First, we keep the number of OpenMP “critical regions” to an absolute minimum and instead rely on “atomic” constructs. Second, we use many more tasks per MPI rank than there are hardware threads, which makes for many more executable tasks than there are neighbour dependencies. Intra-node scalability is therefore in general limited only by memory bandwidth and cache usage.

In what follows, we describe the fundamentals of the DISPATCH simulation framework. In Section 2, we describe the overall structure of the framework, outlining its constituent components and their interaction. In Section 3, we review the code structure in the context of the execution of an experiment. In Section 4, we describe some of the code components of the DISPATCH framework in detail. In Section 5, we validate the concept by demonstrating, using four different numerical experiments, that the codes employed produce the same results as when used separately, using the examples to also explicitly demonstrate some of the framework advantages. To emphasize the framework aspect, each of the experiments uses a different solver; two internal solvers (a hydrodynamical Riemann solver and a staggered-mesh RMHD solver) and one external solver (ZEUS-3D, implemented as an external library). Finally, in Section 6, we summarize the properties and advantages of the DISPATCH framework, relative to using conventional codes such as RAMSES, STAGGER, and AZEuS. In follow-up papers (Popovas et al, Ramsey et al., in prep.), we will extend our description of the DISPATCH framework to include dynamic refinement, moving patches and patches of mixed coordinate types.

## 2 OBJECT HIERARCHY

DISPATCH is written in object-oriented Fortran and relies heavily on the concept of inheritance<sup>3</sup>, using two main classes of objects; *tasks* and *task lists*. Obviously, the DISPATCH ideas and concepts could easily be carried over to

<sup>2</sup> <https://ccse.lbl.gov/BoxLib/index.html>

<sup>3</sup> In Fortran “objects” are called “data types”, and inheritance is implemented via “data type extensions”

any other object-oriented language, such as C++, but conversely Fortran does not impose any serious language related limitations on the implementation of the concepts.

## 2.1 Tasks

The task class hierarchy has as its defining member a

(i) *task* data type, which carries fundamental state information such as (double precision) task positions, task times, time steps, status bits, etc. Mesh based task are all extensions of the task data type to a

(ii) *patch* data type, which adds information about the mesh, such as size, resolution, number of guard zones, number of time slices saved for time interpolation, mesh type (Cartesian or curvi-linear), etc. These are generic properties, shared by all mesh based

(iii) *solver* data types, which add methods to advance the patch data forward in time, plus any parameters and the like that are specific to the solver in question. The specific solver data type is then extended to a generic

(iv) *experiment* data type, which adds experiment specific functionality, such as initial and boundary conditions, and also serves to hide the choice of solver, making it possible to execute the same experiment with different solvers. The experiment data type also serves to create a generic layer that can be accessed from the *task list* class hierarchy, independent of the type of solver that is actually used by the experiment.

## 2.2 Task lists

The *task list* class hierarchy has as its defining member a

(i) *list* data type, which defines a doubly-linked list of nodes that carry information about tasks. In addition to pointers to the previous and next nodes, the nodes in the list have pointers to the associated tasks, and to linked lists of *nbors*; a concept that generalizes neighbours to include tasks that in one way or another relate to the main node task; either because they depend on the task, or because the task depends on them. The list data type contains the generic procedures necessary to manipulate linked lists, while the

(ii) *task list* data type extends the list data type with procedures that are specific to the handling of task relations. In particular, the task list data type contains the *update* procedure, which is a key procedure in DISPATCH, responsible for selecting task for updating. The complete execution of a DISPATCH experiment essentially consists of calling the task list *execute* procedure, which calls the task list *update* procedure repeatedly, until all tasks have advanced to their final `task%end_time`.

## 2.3 Components

Task lists, in turn, may be generated by a set of scene *components*, which produce collections of tasks, organized in some systematic fashion. One of the basic members of this hierarchy is the *cartesian* component, which has tasks organized in a Cartesian arrangement, with each task in general having nbors in three Cartesian directions. The corresponding mesh-based tasks (patches) may, in turn, have Cartesian

or curvi-linear coordinates; in the latter case the Cartesian component arrangement of tasks is one in index space.

Other already existing components have *Rubik's Cube* or *Rubik's Revenge* arrangements of patches. The former arranges 27 patches into 3x3x3 groups, and then repeats the arrangement recursively, by splitting the central patch into 3x3x3 child patches, each with cell sizes that are three times smaller than in the previous level of the hierarchy. The arrangement may be continued recursively, possibly complemented at the largest scales with repetitions of the topmost arrangement in one or more directions.

The *Rubik's Revenge* component is analogous, except it uses 4x4x4 patches, where the central 2x2x2 patches are split into a new 4x4x4 arrangement, leading to a hierarchy with a factor of two decrease in patch size for each level of the hierarchy.

The Rubik's type components are useful for example for representing the environment near a planet embryo in an accretion disk, making it possible to cover the scale range from a small fraction of the planet radius to the scale height of the accretion disk with a relatively limited number of patches (e.g.  $(N_{\text{level}} + N_{\text{extra}}) \times 27$ ). The whole Rubik's component then consists of patches that are co-moving with the planet embryo, thus gaining a time step advantage relative to fixed mesh codes similar to that of Fargo (Masset 2000) and 3D-Fargo (Benítez-Llambay & Masset 2016). The patches can be made to rotate, so as to keep one direction always pointing towards the center of the accretion disk, with corresponding Coriolis and net inertial (centrifugal) forces added to the solver.

## 2.4 Scenes

*Components* such as the ones exemplified in the previous subsection may be used as building blocks in a *scene hierarchy*, where one could have, for example, a top level that is a *galaxy model*, which in its spiral arms contain a number of instances of *giant molecular cloud* components, each of which contains any number of *accretion event* components, where an accretion event component contains an accretion disk component, with a collection of freely moving patches representing the gas and dust of the accretion disk. These patches would be circling a central star, whose evolution could be followed by a MESA (Paxton et al. 2010) -task, taking accretion rates directly from a sink particle recipe running in the central patch. In addition, the accretion event component could contain Rubik's Cube components, co-moving with planet embryos, possibly created through non-axisymmetric evolution of dust traps, which would in turn be coupled to the thermal processing and particle transport tasks mentioned below.

In this and other scenes and scenarios, radiative energy transfer tasks could be operating, either as sub-tasks inside other tasks, or as semi-independent separate tasks, coupled more loosely to patches servicing physical conditions, while conversely being serviced by results from the radiative transfer tasks. It is, for example, already common practice in BIFROST (Gudiksen et al. 2011) solar simulations to solve the radiative transfer problem with a different cadence / time step than the one used when evolving the MHD (Hayek et al. 2010).

Likewise, particle tasks could be operating, either

as sub-tasks inside other tasks, or as semi-independent separate tasks. These would then be able to use data on gas and dust properties from accretion disk patches to estimate the production rate of thermally processed components — representing for example chondrules and high-temperature-condensates (calcium-aluminum inclusions, amoeboid olivine aggregates, hibonites, ...; cf. Haugboelle et al. 2017), and would be able to model the subsequent transport of thermally processed components by disk winds and jet outflows (Bizzarro et al. 2017).

### 3 CODE FUNCTIONALITY

The overall structure and functionality of the code framework is best understood by combining several possible perspectives on the activities that take place as an experiment is executed. Below we adopt, one-by-one, perspectives that take A) the point of view of a single task, and the steps it goes through cyclically, B) the point of view of the task scheduler / dispatcher, as it first selects tasks for execution / updating and then later checks back on these tasks to evaluate the consequences of the updates. Then C) we take the point of view of looking at the ensemble of MPI processes, and their means of communicating. Next D), we take the point of view of the load balancer, and look at how, in addition to keeping the load balanced between the MPI processes, it tries to keep the actual need to communicate as low as possible. Finally E), we take the point of view of the I/O sub-system, and look at how snapshots of the task update process in the MPI processes can be written out to disk, for post-processing and/or experiment continuation.

#### 3.1 A) Single task view

To be specific, we consider the phases that a mesh-based *experiment* task goes through. Such a task, which is an extension of a *solver* task, relies on having guard zone values that are up-to-date, before it can be updated. Before the guard zone values are in place the task is in a “not ready” state, while after the guard zone values are in place it is in a “ready” state. In general guard zone values have to be interpolated in time, since patches use local time stepping. Patch values are therefore saved in a number of time slices (typically 5-7), using a circular buffer. The dispatcher checks if neighbouring patches have advanced enough to supply guard zone values, before moving a task onto a (time sorted) ready-queue, from which it then selects the oldest one when a thread becomes available. After having been selected by the dispatcher for update, tasks are then switched to an “updating” state, in which both the internal state variables (e.g. 8 MHD variables) are updated, and the patch time is updated. The new state variables overwrite the oldest state variables in the circular buffer, which typically brings the task back to the “not ready” state, with guard zone values corresponding to the new time not yet available. Occasionally, when the time advance has brought the task past its next scheduled *out\_time*, a patch output procedure (generic to the patch data type or overloaded by a solver or experiment specific output procedure) is called (see below).

#### 3.2 B) Task scheduler view

In the series of states and events discussed above, the selection and preparation of the task for update is the responsibility of the task scheduler *update* procure, which is a central functionality (in practice spread over several procedures) in the DISPATCH code – this is essentially the *dispatcher* functionality that has given the code framework one of the interpretation of its name (the other one being derived from its use of partially DISconnected PATCHes).

The task list update procedure can operate in two modes. It can either

- (i) Let the threads pick the oldest task from a linked list (a “ready queue”) of tasks that have been cleared for update. This linked list is sorted by time (oldest first), so a thread only has to pick off the head from the queue and execute its update procedure. In this scheme, the thread also immediately checks the neighbours of the updated task to see if perhaps one of those tasks became “ready”, e.g. because the updated task is able to provide the last piece of missing guard zone data. Any “ready” tasks that are found are entered into the “ready queue”, in time order. Alternatively,
- (ii) the task list update procedure runs on a single OpenMP thread, picks off the oldest task from the ready queue and spawns a thread that updates it. It then searches the neighbour list for tasks that possibly became executable, and adds these tasks to the ready queue.

The first alternative is the simpler one, but has the drawback that two of the linked list operations — picking off the head of the ready queue and adding new tasks to the ready queue are continuously being performed by a large number of threads in parallel. These two operations must therefore be protected with OpenMP critical regions, to make sure that only one thread at a time is allowed to manipulate the ready queue. This is not a problem as long as the number of threads per MPI-process is limited; even on a 68-core KNL processor there is hardly any measurable impact.

However, in order to truly obtain unlimited OpenMP scalability it is necessary to operate entirely without OpenMP critical regions, which is possible with the second mode of operation of the task list update procedure. In this mode, a single (master) thread is responsible for both removing tasks from the ready queue, as well as for adding new tasks to it. In this mode, the actual task updates are performed by OpenMP task constructs, with the task list update procedure running on the master thread being responsible (only) for spawning tasks and handling linked list operations. Therefore, no critical regions are needed, and one can reach much larger numbers of threads per MPI process. The load on the master thread is expected to be ignorable, and if it ever tended to become noticeable, it can easily spawn subtasks that take care of most of the actual work. Note also that the default behaviour of OpenMP task constructs is that the spawning task can also participate in the actual work (possible encouraged to do so by suitably placed `$omp taskyield` constructs).

#### 3.3 C) MPI process view

An MPI process typically runs on either all cores on a compute node, or else on all cores on a “socket”, engaging a num-

ber of OpenMP threads that typically exceed the number of available physical cores (to achieve some degree of “hyper-threading”). Since the number of tasks that are executable at any given time may be a small fraction of the total number of tasks, each MPI process must typically “own” a number of tasks that significantly exceeds the number of available OMP threads / cores. Some of these tasks (“boundary tasks”) have neighbour tasks (“virtual tasks”) that belong to a different MPI process, while other (internal) tasks have neighbours that are all owned by the same MPI process.

As soon as a boundary task has been updated, an MPI package is prepared and is sent to all MPI processes that need information from that task, typically for supplying guard zone values. By sending this information pro-actively, rather than having the other MPI-processes ask for it, latency can be greatly reduced, and chances improve that the boundary patches of other MPI processes will have guard zone data available in their virtual patch neighbours, at the points in time when their neighbour lists are checked.

Boundary patch data are sent to neighbour MPI-processes in the form of a “package”, which contains both a copy of the most relevant task parameters, and the dynamical 3-D variables in the interior of the patch. For mainly two reasons data for the whole interior is shipped, rather than limiting the package content to only the layers that may be needed for guard zone data. First, this simplifies the package handling, and network capacity is generally large enough to support this, without noticeable slowdown. Secondly, this simplifies load balancing, since it allows changing the owner of a patch by simply “giving” a patch to a neighbour MPI-process. The patch then only needs to change status, from “virtual” to “boundary” on the receiver side, and from “boundary” to “virtual” on the sender side.

Should memory bandwidth actually become a problem one can reduce the network traffic significantly, by only sending guard zone values, at the cost of added complexity in the package pack and unpack procedures and in the load balancing procedures.

### 3.4 D) Load balancer view

Given the ownership swap protocol outlined above, the actual balancing of work load is a near-trivial task, since any MPI-process that finds itself overloaded by work, relative to a neighbouring MPI-process, can easily “sell” some of its boundary patches to its less loaded neighbour MPI processes. However, doing so indiscriminately risks creating too ragged boundaries between neighbouring MPI-processes. In this sense, the procedure handling load balancing should also function as a “communication balancer”, which tries to keep the number of communications needed per unit simulation time near a minimum value.

By emulating an initially and severely fragmented patch distribution through software prototyping, we found that a good approach is to address the load imbalance and the communication reduction in two separate steps, where in each step the other aspect of the balancing is more or less ignored.

The procedures are essentially as follows:

- (i) Count the number of MPI-neighbours for each rank, by

counting the total number of different ranks in the neighbour lists of its boundary patches.

- (ii) Evaluate, for each boundary patch, if the number of MPI-neighbours would be reduced (accounting for changes on both ranks) if ownership was swapped. In this step one carries out the most advantageous swaps, even if the swaps would tend to introduce load imbalance.

- (iii) In a separate step, evaluate if swaps can be made that restore load balance, without increasing the number of MPI-neighbours.

The reason this two step procedure is advantageous, relative to trying to reduce communications under the simultaneous constraint to not cause imbalance, is that it is relatively difficult to find good swaps in step 2), and the process made is easier if load balance is ignored, while it is relatively easy in step 3) to find swaps that restore load balance without changing the total number of of MPI-neighbours.

### 3.5 E) Input/Output view

After a task has been updated, its current time in code units is checked against the time `task%out_next`, which is a parameter in the task data type. On passage of that time, the `experiment %output()` procedure is called. If no experiment specific procedure has been specified in the experiment module, the call is intercepted by a generic patch module output procedure. Currently, this supports two output formats: One that writes patch data as raw binary data to one file, and patch information as text to another file. An alternative output format uses the packing procedure used to communicate patch data between MPI nodes, collecting these into a single file per MPI process. Future HDF5 support is anticipated.

## 4 CURRENT CODE COMPONENTS

### 4.1 Internal and external HD, MHD, and PIC solvers

Solvers from various available external codes have been carried over to the DISPATCH framework, and have been validated via comparisons with experiments carried out with the original codes. As a first representative of Riemann solvers, the HLLC solver from the RAMSES public domain code (Teyssier 2002) has been incorporated, and to be able to take advantage of the DISPATCH speed advantages in stellar atmosphere and similar work (Baumann et al. 2013), several versions of the Stagger Code (Nordlund et al. 1994; Kritsuk et al. 2011) class of solvers have also been carried over. As an example of connecting to an external solver, implemented via an interface and library calls, the ZEUS-3D solver (Clarke 1996, 2010) used in the AZEuS adaptive mesh refinement code (Ramsey et al. 2012) has also been incorporated. The ZEUS-3D solver is the only currently-included solver that can take advantage of orthogonal, curvilinear coordinate systems (e.g. cylindrical, spherical).

In ongoing work we are also incorporating the public domain (`bitbucket.org`) PPcode version of the photon-plasma particle-in-cell code (Haugbølle et al. 2013), as well as the BIFROST code (Gudiksen et al. 2011), with all of its modules related to chromospheric and coronal physics. These solvers will be used in a multiple-domain-multiple-physics

experiments, for modelling solar and stellar atmospheric dynamics driven by sub-surface magneto-convection, expanding on the type of work exemplified by [Baumann et al. \(2013\)](#).

## 4.2 Radiative transfer

Radiative processes are undeniably important in most astrophysical applications (star and planet formation, ionization in HII regions, solar and stellar activity, and radiative heating from stars to name a few). Being a 7-dimension problem (3-space + time + wavelength + space angle) it is a daunting physical process to solve. There are a number of different approaches to tackle the problem, such as flux-limited diffusion (FLD, e.g., [Kuiper et al. 2010](#)), Fourier transforms (e.g. [Cen 2002](#)), short (e.g. [Stone et al. 1992](#)), long (e.g. [Nordlund 1982](#); [Heinemann et al. 2006](#)) and hybrid (e.g. [Buntemeyer et al. 2016](#)) characteristics ray-tracing. DISPATCH uses a hybrid-characteristics ray-tracing scheme (long rays inside patches, short rays in between, with some exceptions, explained below).

The radiative transfer (RT) package consists of a ray geometry component, an initialization component, and runtime schemes. Each of them needs to know very little of how the rest are working, while they rely heavily on each other. Below we briefly explain the purpose of each of these components. They will be described in detail, together with implementation for refined-meshes, in a subsequent paper of this series ([Popovas et al., in prep.](#))

### 4.2.1 Ray geometry

When the RT package is initialized it first sets up ray-geometry (RG) for all the patches. The only information the RG component needs is the simulation geometry type (Cartesian/cylindrical/spherical), dimensions of a patch (number of cells per direction), the number of ray-directions, and their angular separation. The RG component then proceeds in spawning the rays. Each ray starts at one of the patch boundaries and ends at some other boundary (face, edge, or corner) of the same patch. Rays are separated from one another by one cell size (in the "most perpendicular direction") and the ray points are, ideally, cell-centred along the direction of the ray. In such a case the required hydrodynamic quantities, such as density and internal energy, do not need to be interpolated, and the resulting intensities do not need to be interpolated back to the mesh, saving significant amounts of computational time.

After all rays are spawned they are organized into a quick look-up tree hierarchy:

(i) *Ray geometry* type (Cartesian/cylindrical/spherical) is the first key when browsing through the rays. The rays are further divided into

(ii) *ray directions* - in principle, as long as scattering is not considered, rays in one direction do not care about rays going in other directions, so they can be separated out and passed on to as independent tasks to different threads. To solve for an RT solution inside a patch one needs boundary conditions from the walls that the rays originate from. Not all slanted rays in one direction originate and terminate at the same walls (see figure 1 for a 2-D example). To avoid

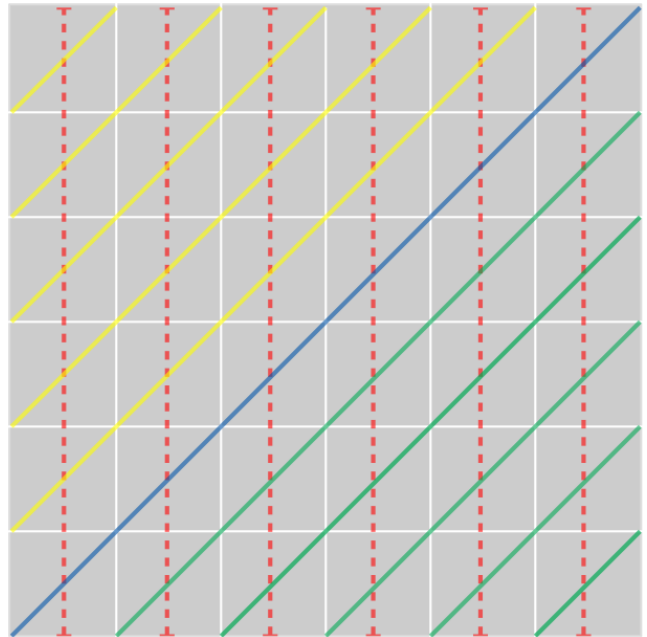


**Figure 1.** Ray geometry representation in 2-D. (M)HD grid cells are represented by grey squares, colored lines represent rays. Different line styles represent different directions. Different colors represent different bundles.

waiting time originating from more than one boundary wall the directions are further subdivided into

(iii) *ray bundles*. These are the sets of rays that originate and terminate at the same set of walls. RT is a highly repetitive task, where typically large numbers of rays are considered. It is thus highly advantageous to use schemes that allow vectorization, to reduce the computation time. To maximize the vectorization efficiency, all rays should preferably be of the same length. This is a natural feature of axes-oriented rays, while slanted ones need to be further rearranged into

(iv) *ray packets*. These are the sets of rays in one bundle that have the same length. For faster data lookup (ray point coordinates on a mesh, origin/termination points, etc.), they are organized as data arrays.

Axis-oriented rays, as well as rays with particular inclinations (e.g.  $45^\circ$ ) tend to terminate at locations that coincide with points of origin of rays in the downstream patch. This is exploited by introducing the concept of *ray bundle chains*.

### 4.2.2 Ray bundle chains

To get correct heating/cooling rates inside a patch one needs boundary values / incoming intensities from upstream patches, or boundary conditions. Ray reorganization into bundles minimizes the number of walls needed per particular bundle down to one. Such an arrangement allows one to connect the rays in particular bundles to a similar set of rays in another bundle, belonging to a different patch, creating a *chain of bundles*. If we consider these chains being actual chains, the master (first) chain link is connected to some outer boundary, all the other links in the chain

can get their boundary values from the upstream link, instantaneously after it is produced. These chains effectively transform the short-ray scheme in-between patches into long rays over many patches along the ray direction. The actual method of bundle connection is beyond the scope of this paper and will be explained in a subsequent paper of this series.

#### 4.2.3 RT initialization

After the ray geometry has been generated the RT initialization component goes through all the patches in the task list and creates an overlapping rt-patch for each (M)HD patch. The rt-patch knows about all the ray-directions, and sets up the bundle chains by browsing through its neighbour patches to find the upstream ones. If the upstream surface is an internal/external boundary, or a change of the level or refinement, the particular bundle chain link is defined as being the master link, i.e. the one from which the RT execution starts.

#### 4.2.4 RT execution

When the (M)HD patch is updated and the internal hydrodynamic quantities become available, the rt-patch is ready to be executed. Initially it may not have wall data available, but can still prepare the internal part — evaluating the source function and opacities for all the internal cells. It then goes through the its list of bundles and nudges the master links of all the bundle chains. The master link might belong to this patch, or it may belong to a very distant patch along the ray direction. In most cases, all links along some arbitrary ray direction are not ready (internal data for some rt-patches are not prepared yet), so the master link in the chain just updates its status, indicating which links in the chain are prepared. As soon as a last nudge indicates that all the links are ready, the chain can be executed, recursively:

(i) the first bundle in the chain takes the boundary values either from boundary conditions, or maps them from an upstream patch, which is either a virtual patch or has a different refinement level;

(ii) at the same time the source function and opacities are mapped from internal data onto the bundle, in temporary arrays;

(iii) boundary values and internal data is sent to an RT solver (using an integral or Feautrier method, e.g. Nordlund 1984), which returns the heating/cooling rates for internal cells as well as boundary intensities, which in turn are sent to the next link in the bundle-chain.

A validation benchmark is presented in Section 5 below. Additional details and benchmarks, aimed at documenting the accuracy and speed of the radiative transfer implementation, will be presented in a subsequent paper of this series (Popovas et al., in preparation).

### 4.3 Non-ideal MHD

Non-ideal MHD effects (Ohmic dissipation, ambipolar diffusion and Hall effect) occur in various astrophysical context, such as for instance in protoplanetary disks and the interstellar medium. We account for the effects of Ohmic dissipation

and ambipolar diffusion by extending the standard MHD solvers that have been implemented in DISPATCH with the additional effects caused by non-ideal MHD. We illustrated the process with the staggered mesh class of solvers derived from the Stagger Code (Nordlund et al. 1994; Kritsuk et al. 2011).

The implementation in different solvers differ mainly in details related to the centring of variables. In the STAGGER and ZEUS-3D solvers, mass density and thermal energy / entropy are volume-centred, components of linear momenta and magnetic fields are face-centred, while electric currents and electric fields are edge-centred.

#### 4.3.1 Ohmic dissipation

Ohmic dissipation results from the additional electric field that is induced by the imperfect conduction in a magnetized fluid. For simplicity, we assume an isotropic resistivity that can be described by the scalar parameter,  $\eta_{\text{Ohm}}$ , and write the additional electric field as

$$\mathbf{E}_{\text{Ohm}} = \eta_{\text{Ohm}} \mathbf{J}. \quad (1)$$

A non-zero resistivity also causes an additional heating term  $Q_{\text{Ohm}}$  due to Ohmic heating

$$Q_{\text{Ohm}} = \mathbf{J} \cdot \mathbf{E}_{\text{Ohm}} = \eta_{\text{Ohm}} J^2. \quad (2)$$

We (separately) recentre the corresponding vector components of the electric current and the electric field to cell centre to compute the cell centred heating rate.

Additionally, we adjust the time step criterion by adding the constraint

$$\Delta t \leq \Delta t_{\text{Ohm}}, \quad (3)$$

where we use the following expression for  $\Delta t_{\text{Ohm}}$  of Masson et al. (2012)

$$\Delta t_{\text{Ohm}} = C_{\text{Ohm}} \cdot \min \left( \frac{\Delta x^2}{\eta_{\text{Ohm}}} \right). \quad (4)$$

$C_{\text{Ohm}}$  is a Courant-like parameter, conservatively chosen = 0.1 by Masson et al. (2012).

#### 4.3.2 Ambipolar diffusion

In the case of a gas that is partly ionized and partly neutral, a magnetic field directly affects the ionized gas but not the neutral gas, which instead is coupled to the ions via ion-neutral drag. In general, therefore, the ionized gas moves with a different speed than the neutral gas. If the speed difference is small enough to neglect inertial effects the effect can be represented by estimating the speed difference (drift speed) of the ionized gas relative to the neutral gas. We implement this 'single-fluid approach' along the lines of previous works (cf. Padoan et al. 2000; Duffin & Pudritz 2008; Masson et al. (2012)).

Specifically, we add an additional ambipolar diffusion electric field

$$\mathbf{E}_{\text{AD}} = \mathbf{v}_D \times \mathbf{B} \quad (5)$$

to the induction equation, where

$$\mathbf{v}_D = \frac{1}{\gamma_{\text{AD}} \rho \rho_i} \mathbf{J} \times \mathbf{B} \quad (6)$$

is the drift velocity, and  $\gamma_{AD}$  is the *ambipolar drift coefficient*.

The ambipolar drift also causes an additional heating term

$$Q_{AD} = \rho_i \rho \gamma_{AD} (\mathbf{v}_D)^2. \quad (7)$$

In staggered mesh solvers we recentre the velocity and magnetic field components to edges when computing  $\mathbf{E}_{AD}$ , and recentre the drift velocity components to cell centres to compute  $Q_{AD}$ .

Similar to the implementation of Ohmic dissipation, we also add a constraint on the time step, so that (cf. [Masson et al. 2012](#))

$$\begin{aligned} \Delta t &\leq \Delta t_{AD} = C_{AD} \min \left( \frac{\gamma_{AD} \rho_i (\Delta x)^2}{v_A} \right) \\ &= C_{AD} \min \left( \frac{\gamma_{AD} \rho_i \rho}{\mathbf{B}^2} (\Delta x)^2 \right) \end{aligned} \quad (8)$$

with  $C_{AD}$  conservatively chosen as 0.1.

#### 4.4 Equation-of-state and opacity tables

Lookup tables with equation-of-state and opacity data are generated in Python and are passed on to DISPATCH as binary data files. The Python code reads data from public sources — typically in text format — and converts it into tables with the (log of) the primary density and energy variables used in the various solvers as independent variables. The HLLC and ZEUS-3D solvers use thermal energy, as does several of the Stagger Code solvers, while one version of the Stagger Code solvers instead uses entropy as the energy variable.

The table lookup is heavily optimized, first by using spline interpolations in Python to produce tables with sufficient resolution to use bi-linear interpolation in DISPATCH. The table address calculations and interpolations are vectorized, with only a small (data access) fraction of the procedure remaining non-vectorized (necessary because of indirect addressing).

## 5 VALIDATION EXAMPLES

Several of the solver components of the framework are copies of solvers from existing, well-documented codes, and validation in the DISPATCH context then requires only verification that results agree with those from the existing codes, and verification that the partitioning into patches with independent time steps does not change results significantly. In this section we document validation tests for the main HD and MHD solvers, for the non-ideal MHD extension to these solvers, and for the radiative transfer code component. We concentrate on the validation aspect, mentioning performance and scaling only in passing; more details on these aspects will appear in a subsequent paper ([Ramsey et al, in prep.](#)).

All solvers share a set of standard initial conditions (sound waves, magneto-sonic waves, driven turbulence, etc.), which are used to validate the solvers against each other, and to check functionality and reproducibility after updates of the code framework. A simple validation mechanism has been implemented, which allows each experiment to be validated, relative to previous results, by simply giving the

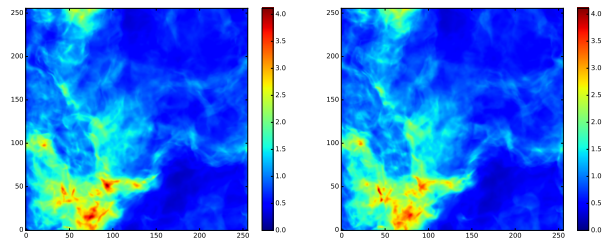


**Figure 2.** *Left:* Projected density at time  $t = 0.2$  for the decaying turbulence experiment, when using a single  $256^3$  patch. *Right:* The same, when using 512 patches with resolution  $32^3$ .

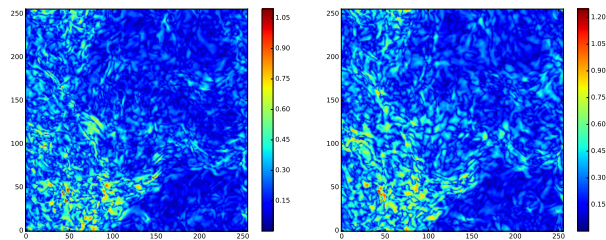


**Figure 3.** *Left:* The absolute difference between the left and right images in Fig. 2. *Right:* The difference between two solutions, obtained with Courant numbers 0.6 and 0.8, respectively.

Linux command `validate`. Selected experiment validations are also triggered whenever an update is pushed to the code GIT repository, using the ‘pipeline’ feature at [bitbucket.org](#).

### 5.1 Decaying supersonic turbulence

To demonstrate that solvers in the DISPATCH framework match results from the same solvers in existing codes, we use the decaying turbulence experiment from the KITP code comparison ([Kritsuk et al. 2011](#)). The experiment follows the decay of supersonic turbulence, starting from an archived snapshot with resolution  $256^3$  at time  $t = 0.02$ , and following the evolution until code time  $t = 0.2$ .

In Fig. 2 we display the projected mass density at the end of the experiment, carried out using the HLLC solver from RAMSES, using on the one hand (left panel) a single patch (reproducing results obtained in RAMSES), and on the other hand (right panel) using 512 patches with resolution  $32^3$ , evolving with local timesteps determined by the same Courant conditions as in the RAMSES code, but locally, for each patch. The figure shows that the solutions are visually nearly indistinguishable, even after what amounts to about two dynamical times. The root-mean-square velocities are practically identical, with a relative difference of only  $6 \cdot 10^{-4}$  at the end of the experiments.

Figure 3 shows two difference images, displaying the absolute value of the differences (raised to the power 0.5 to enhance visibility). The left hand side panel shows the difference between the runs with 1 and 512 patches, while the right hand side panel shows the difference between two otherwise identical cases, run with slightly different Courant numbers (0.6 and 0.8). The panels illustrate that a turbulence experiment can never be reproduced identically, except when all conditions are exactly the same; small differences

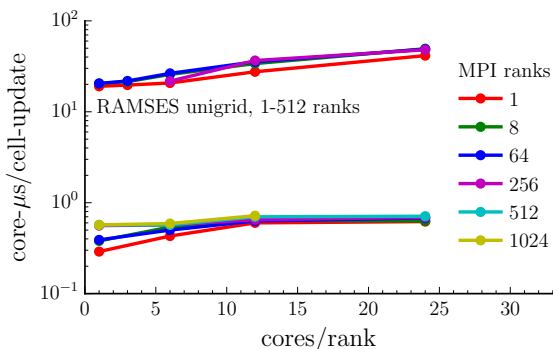


**Figure 4.** Strong and weak scaling for DISPATCH with the RAMSES HLLC solver, as compared to the version of RAMSES (with HLLD) used in the zoom-in simulations of Nordlund et al. 2014.

due to truncation errors grow with time, according to some Lyapunov exponent.

The figure validates the use of our patch based local time stepping in two different ways; first through the absence of any trace of the patch boundaries in the difference image, and secondly by demonstrating that the differences are consistent with differences expected from just the use of different Courant numbers. Local regions with relatively low flow speeds are effectively evolved with very low local Courant numbers in the single patch case (as well as in the RAMSES code), while the patch based evolution takes advantage of the lower speeds by using locally larger time steps.

The local time step advantage may be quantified by the number of cell-updates needed. The single patch case needs about  $2 \cdot 10^{10}$  cell updates (as does the RAMSES code), while the experiment using 512 patches with local timesteps needs only about  $1.4 \cdot 10^{10}$  cell updates. On our legacy cluster nodes, with 20 core Ivy Bridge CPUs, the complete experiment takes only 6.5 minutes when run on 30 hardware threads (7.0 minutes with 20 threads). The cost per cell update is 0.61 core microseconds in the single patch case, 0.56 core-microseconds in the 20 thread case, and 0.53 core-microseconds in the 30 thread case). The super-linear scaling from 1 to 20 cores is mainly due to better cache utilization in the  $32^3$  patch case, while the additional improvement when using 30 hardware threads on 20 cores illustrates the *hyper-threading* advantage; with more hardware threads than cores the CPU has a better chance to find executable threads.

### 5.1.1 Weak and strong scaling

We have used simple experiments with driven turbulence to explore weak and strong scaling on clusters with legacy Intel and KNL CPUs (cf. Fig. 4), finding, as in the decaying turbulence case, typical cell update costs of order 0.5 core-microseconds, while on the somewhat slower Knight Landing (KNL) cores the update cost is about 1.0 core-microseconds.

## 5.2 Non-ideal MHD: C-shock

To validate the non-ideal MHD component, we carry out the Masson et al. (2012) C-shock experiment, for both Ohmic

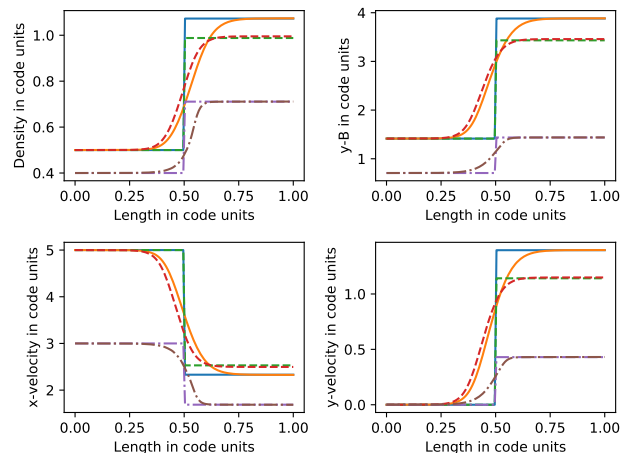


**Figure 5.** Density (upper left),  $B_y$  (upper right),  $v_x$  (lower left) and  $v_y$  (lower right) for the three C-shock experiments. The solid lines correspond to the initial (blue) and evolved state (orange) of the isothermal run, the dashed-dashed lines correspond to the initial (green) and evolved state (red) of the non-isothermal run, the dashed-dotted lines correspond to the initial (dark violet) and evolved state (purple) of the Ohmic dissipation run.

dissipation and ambipolar diffusion. Table 1 shows the initial conditions on the two sides of the shocks. In the isothermal case, we set the adiabatic index  $\gamma = 1 + 10^{-7}$ , while we use  $\gamma = 5/3$  for the non-isothermal and the Ohmic dissipation run. To check whether the variables are placed on the correct locations in the cell, we test the implementations on a single patch with dimensions  $128 \times 4 \times 1$  and plot the shock for a 1D slab of  $128 \times 1 \times 1$  in size (Fig. 5). In agreement with the tests by Masson et al. (2012) and Duffin & Pudritz (2008), the shock undergoes a brief period of adjustment before the shock reaches a steady state solution for the three cases.

## 5.3 Radiative transfer: Shadow casting benchmark

To test our implementation of radiative transfer we use a shadow casting benchmark (Jiang et al. 2012, Ramsey & Dullemond 2015). We consider a 3-D Cartesian domain of size  $-0.5 \leq [x, y, z] \leq 0.5$  cm. An overdense ellipsoid is centred at the origin, with a density profile prescribed by:

$$\rho(x, y, z) = \rho_0 + \frac{\rho_1 - \rho_0}{1 + e^{10(r-1)}}, \quad (9)$$

where  $r = (x/a)^2 + (y/b)^2 + (z/b)^2$ ,  $a = 0.01$  cm,  $b = 0.06$  cm, and  $\rho_1 = 10\rho_0$ . The ambient medium is initialized to a gas temperature of  $T_0 = 290$  K and a density  $\rho_0 = 1$  g cm $^{-3}$ . The entire domain is in pressure equilibrium. The gas opacity is given by:

$$\alpha = \kappa\rho = \alpha_0 \left(\frac{T}{T_0}\right)^{-3.5} \left(\frac{\rho}{\rho_0}\right)^2, \quad (10)$$

where  $\alpha_0 = 1$ . We set a constant and uniform irradiation source across the left boundary (at  $x = -0.5$  cm), characterized by blackbody emission with effective temperature  $T_{irr} = 2000$  K. The other boundaries are assumed to be blackbodies with effective temperature  $T_0$ . For the mesh, we use a  $2^3$  patch set-up, with each patch containing  $64^3$  cells. The

Variable	$\rho$	$v_x$	$v_y$	$B_x$	$B_y$	$P$
Pre-shock	0.5	5	0	$\sqrt{2}$	$\sqrt{2}$	0.125
Post-shock (isothermal)	1.0727	2.3305	1.3953	$\sqrt{2}$	3.8809	0.2681
Post-shock (non-isothermal)	0.9880	2.5303	1.1415	$\sqrt{2}$	3.4327	1.4075
Pre-shock (Ohm)	0.4	3	0	$\frac{1}{\sqrt{2}}$	$\frac{1}{\sqrt{2}}$	0.4
Post-shock (Ohm)	0.71084	1.68814	0.4299	$\frac{1}{\sqrt{2}}$	1.43667	1.19222

**Table 1.** Parameters of the C-shock experiment for non-ideal MHD validation. Pre-shock (upstream) values refer to the left hand side in the figure panels.

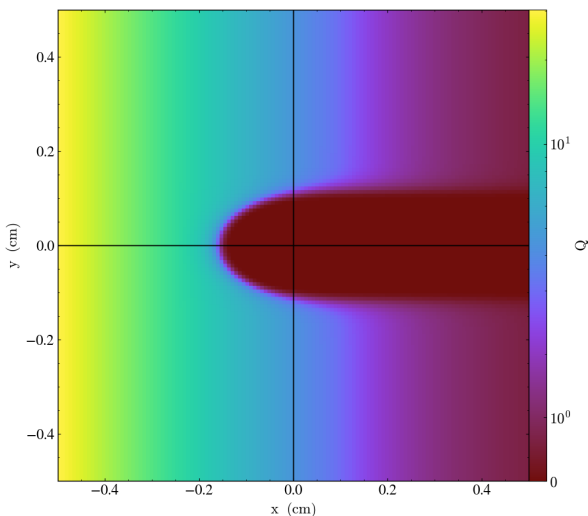


**Figure 6.** Results from shadow casting benchmark. The irradiation source is located at the left boundary. The heating  $Q$  is steadily decreasing, until it reaches 0 at the right boundary.

ray geometry contains 13 directions with  $45^\circ$  space-angle separation. In this set-up, the ambient medium is optically thin and the photon mean free path of the axes-oriented rays is equal to the length of the domain. The clump is optically thick, with an interior mean free path of  $\approx 3.2 \cdot 10^{-6}$  cm. The clump thus absorbs the irradiation incident upon it, and casts a shadow behind it. Figure 6 shows the result. As can be seen, the shadow is sharp and realistic (slightly increasing in width when moving away from the source of irradiation). The heating  $Q$  reaches 0 (ambient temperature) at the right end of the simulation box.

#### 5.4 de Val-Borro disk benchmark

One of the current and primary science goals of DISPATCH is to model planet formation processes in global and realistic settings. As such, we now apply DISPATCH to the global disk benchmark of de Val-Borro et al. (2006). More specifically, we embed a Jupiter-mass planet in an initially uniform surface density protoplanetary accretion disk and then allow the disk to evolve for 100 orbits at the semi-major axis of the planet. Following de Val-Borro et al. (2006), we initialise a two-dimensional, geometrically thin disk with constant surface density given by  $\Sigma_0 = 0.002M_*/\pi a^2$ , where  $M_*$  is the mass of the central star and  $a$  is the semi-major axis of the

planet. We use an aspect ratio of  $H/R = 0.05$ , where  $H$  is the canonical disk scale height, an effectively isothermal EOS ( $\gamma = 1.0001$ ), and an initial angular velocity which is Keplerian.

In scaled units, the mass of the central star is set to 1.0, while the planet is assigned a mass of  $10^{-3}$  and a semi-major axis of 1.0. The simulation is performed in the reference frame co-rotating with the planet and centred on the central star. Therefore, the gravitational potential of the system is comprised of one term each for the star and planet, plus an additional “indirect” term to account for the fact that the centre-of-mass of the system does not correspond to the origin (cf. D’Angelo & Bodenheimer 2013):

$$\Phi = -\frac{GM_*}{R} - \frac{GM_p}{\sqrt{|R - R_p|^2 + \epsilon^2}} + \frac{GM_p}{R_p^3} R \cdot R_p, \quad (11)$$

where  $G$  is the gravitational constant,  $M_p$  is the mass of the planet,  $R$  is the cylindrical radius,  $R_p$  is the position of the planet in cylindrical coordinates, and  $\epsilon$  is the gravitational softening length. Still following de Val-Borro et al. (2006), we set  $\epsilon = 0.6H$ , and a planetary position of  $(Z, R, \Phi) = (0.0, 1.0, 0.0)$ . In the co-rotating frame, the planet’s position is fixed, i.e. the planet is not permitted to migrate.

The computational domain has dimensions  $[0.4a, 2.5a]$  in radius and  $[-\pi, \pi]$  in azimuth; it is resolved with  $n_R \times n_\Phi = 160 \times 450$  cells. We use polar cylindrical coordinates and the ZEUS-3D solver for this benchmark. When using curvilinear coordinates with ZEUS-3D, it is the angular rather than the linear momentum that is solved, thus guaranteeing the conservation of angular momentum (Kley 1998). Code parameters of note are the Courant factor, which is set to 0.5, and the artificial viscosity parameters (Clarke 2010),  $q_{\text{con}}$  and  $q_{\text{lin}}$ , are set to 2.0 and 0.1, respectively. In the results presented below, a kinematic viscosity of  $10^{-5}$  (in units where  $GM_* = 1$  and  $a = 1$ ) is used.

We adopt periodic boundary conditions in the azimuthal direction, and the “wave-killing” conditions of de Val-Borro et al. (2006) in the radial direction, with damping activated in the ranges  $[0.4a, 0.5a]$  and  $[2.1a, 2.5a]$ . It is worth noting that we do not gradually grow the planet mass over the first few orbits (cf. de Val-Borro et al. 2006; Sect. 3.1), but instead begin with the full planetary mass in place.

The left panel of Figure 7 shows the benchmark results for a single patch at a resolution of  $n_R \times n_\Phi = 160 \times 450$  cells after 100 orbits. These results can be directly and favourably compared with Figure 10 of de Val-Borro et al. (2006). The middle panel, meanwhile, shows the results from subdividing the domain into 45 equally-sized patches. As can be seen, the model with 45 individual patches is nearly identical to the model with a single patch. Finally, the right panel

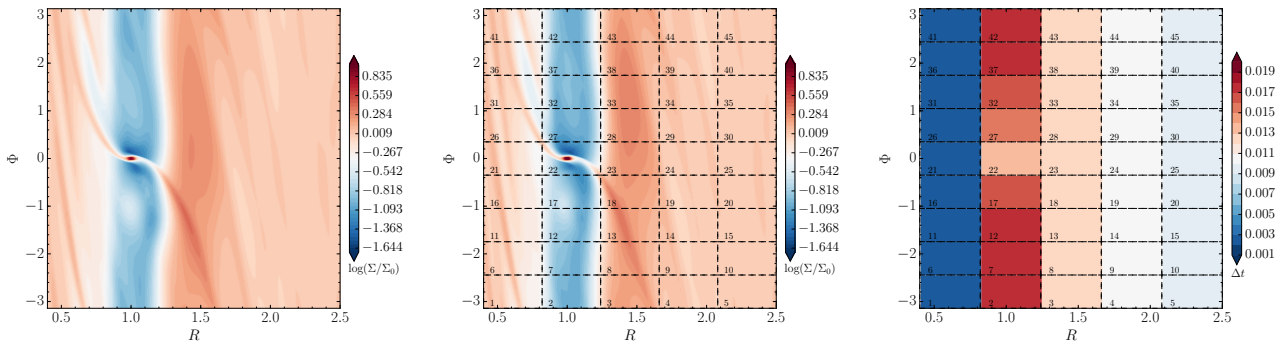


**Figure 7.** *Left:* A  $1M_J$  planet simulated for 100 orbits using a single patch with  $n_R \times n_\phi = 160 \times 450$  uniformly-spaced zones. *Middle:* The same but subdividing the domain into 45 equally-sized patches. *Right:* The time step in each patch after 100 orbits.

illustrates the time step in each patch after 100 orbits; there is a factor of  $\sim 8.2$  difference between the largest and smallest time steps. This local time-stepping advantage, over the course of 100 orbits, reduces the CPU time required by the multiple-patch version by a factor of roughly two relative to the single-patch version ( $\sim 6$  hr vs.  $\sim 12$  hr).

## 6 SUMMARY AND OUTLOOK

We have introduced a hybrid MPI/OpenMP code framework that allows semi-independent task-based execution of code which updates a collection of patches in space-time. OpenMP parallelism is handled entirely by the code framework – already existing code need not (and should not) contain OpenMP parallel constructs beyond declaring appropriate variables as `threadprivate`. OpenMP tasks are generated by a *dispatcher*, which selects the tasks that are ready for, and most in need of, updating (this typically means having valid guard zone data, but can be any type of inter-task dependency). The type of tasks can vary, with ideal MHD, radiative transfer and non-ideal MHD demonstrated here; particle-in-cell (PIC) methods coupled to neighbouring MHD methods are currently in development. Tasks do not necessarily have to be grid based (e.g. particles), while tasks that are may use either Cartesian or curvilinear meshes. Meshes may be stationary or moving. Mesh refinement can be static or dynamic.

As DISPATCH is targeting exa-scale computing, a feature of decisive importance for the overall performance is that time steps are determined by local conditions (e.g. Courant conditions in the case of grid-based tasks); this allows for potentially large reductions in computing time requirements in cases where the signal speed varies greatly within the computational domain. Patches are surrounded by sufficient number of guard zones to allow their interiors to be updated, with guard zone values loaded from neighbouring patches. Since patches evolve on different time scales, it is necessary to save a number of time slices for interpolation (and possibly extrapolation) to the time for which guard zone values are required. Performance, even for existing codes, is augmented when running in the DISPATCH framework, for several reasons: First, patches are small enough to utilize memory caches efficiently, while at the same time being large enough to obtain good vectorization efficiency. Sec-

ondly, task overloading ensures all OpenMP threads remain constantly busy, which results in near-linear OpenMP speed-up, even on nodes with a large numbers of cores (e.g. Intel Xeon Phi KNL). Third, each MPI-process (typically one per socket per node) only communicates with its nearest neighbours – here interpreted broadly, as those MPI-processes that are either geometrically close, or else coupled via, for example, radiation fields. This leads to excellent MPI-scaling. Load balancing is designed to minimize load imbalance while simultaneously keeping the number of communications links near a minimum.

When combined with patches co-moving in, for example, a protoplanetary disk, the advantages relative to a conventional adaptive mesh refinement code such as RAMSES are first of all a large factor from the co-moving patches, with an additional time step advantage that follows from local time stepping. On top of that, there is a substantial raw speed difference per cell update (cf. RAMSES) – mainly due to the much smaller guard zone overhead, but with contributions also from better vectorization and cache utilization.

Planned and ongoing application of the DISPATCH code framework include works on pebble accretion, solar and stellar magneto-convection and atmospheric activity, with further extensions using MHD-PIC multiple-domain-multiple-physics. We plan to make the DISPATCH code framework available in the public domain in a not too distant future.

## ACKNOWLEDGEMENTS

The work of ÅN, MK, and AP was supported by a grant from the Danish Council for Independent Research (DFF). The Centre for Star and Planet Formation is funded by the Danish National Research Foundation (DNRF97). Storage and computing resources at the University of Copenhagen HPC centre, funded in part by Villum Fonden (VKR023406), were used to carry out some of the simulations and analysis presented here. We also acknowledge PRACE for awarding us preparatory access (2010PA3402) to Hazel Hen at HLRS Stuttgart to obtain scaling data.

## REFERENCES

- Adams M., et al., 2015, Chombo Software Package for AMR Applications - Design Document, [http://crd.lbl.gov/assets/pubs\\_presos/chomboDesign.pdf](http://crd.lbl.gov/assets/pubs_presos/chomboDesign.pdf)
- Almgren A. S., et al., 2010, *ApJ*, **715**, 1221
- Baumann G., Haugbølle T., Nordlund Å., 2013, *ApJ*, **771**, 93
- Benítez-Llambay P., Masset F. S., 2016, *ApJS*, **223**, 11
- Berger M. J., Colella P., 1989, *Journal of Computational Physics*, **82**, 64
- Berger M. J., Olinger J., 1984, *Journal of Computational Physics*, **53**, 484
- Berzins M., Luitjens J., Meng Q., Harman T., Wight C. A., Peterson J. R., 2010, in Proceedings of the 2010 TeraGrid Conference. TG '10. ACM, New York, NY, USA, pp 3:1–3:8, doi:10.1145/1838574.1838577, <http://doi.acm.org/10.1145/1838574.1838577>
- Bizzarro M., Wielandt D., Haugbølle T., Nordlund A., 2017, LPI Contributions, **1975**, 2008
- Brandenburg A., Dobler W., 2002, *Computer Physics Communications*, **147**, 471
- Brown D. L., Henshaw W. D., Quinlan D. J., 1997, Overture: An object-oriented framework for solving partial differential equations. Springer Berlin Heidelberg, Berlin, Heidelberg, pp 177–184, doi:10.1007/3-540-63827-X\_59, [http://dx.doi.org/10.1007/3-540-63827-X\\_59](http://dx.doi.org/10.1007/3-540-63827-X_59)
- Bryan G. L., et al., 2014, *ApJS*, **211**, 19
- Buntemeyer L., Banerjee R., Peters T., Klassen M., Pudritz R. E., 2016, *New Astron.*, **43**, 49
- Cen R., 2002, *ApJS*, **141**, 211
- Clarke D. A., 1996, *ApJ*, **457**, 291
- Clarke D. A., 2010, *ApJS*, **187**, 119
- Cunningham A. J., Frank A., Varnière P., Mitran S., Jones T. W., 2009, *ApJS*, **182**, 519
- D'Angelo G., Bodenheimer P., 2013, *ApJ*, **778**, 77
- Dubey A., et al., 2014, *Journal of Parallel and Distributed Computing*, **74**, 3217
- Duffell P. C., MacFadyen A. I., 2011, *ApJS*, **197**, 15
- Duffin D. F., Pudritz R. E., 2008, *MNRAS*, **391**, 1659
- Fromang S., Hennebelle P., Teyssier R., 2006, *A&A*, **457**, 371
- Fryxell B., et al., 2000, *ApJS*, **131**, 273
- Gudiksen B. V., Carlsson M., Hansteen V. H., Hayek W., Leenaarts J., Martínez-Sykora J., 2011, *A&A*, **531**, A154
- Haugboelle T., Grassi T., Frostholm Mogensen T., Wielandt D., Larsen K. K., Vaytet N. M., Connelly J., Bizzarro M., 2017, LPI Contributions, **1975**, 2025
- Haugbølle T., Frederiksen J. T., Nordlund A., 2013, *Physics of Plasmas*, **20**, 062904
- Hayek W., Asplund M., Carlsson M., Trampedach R., Collet R., Gudiksen B. V., Hansteen V. H., Leenaarts J., 2010, *A&A*, **517**, A49
- Heinemann T., Dobler W., Nordlund Å., Brandenburg A., 2006, *A&A*, **448**, 731
- Hopkins P. F., 2015, *MNRAS*, **450**, 53
- Jiang Y.-F., Stone J. M., Davis S. W., 2012, *ApJS*, **199**, 14
- Kale L. V., Bohm E., Mendes C. L., Wilmarth T., Zheng G., 2008, in Bader D., ed., , Petascale Computing: Algorithms and Applications. Chapman & Hall / CRC Press, pp 421–441
- Klein R. I., 1999, *Journal of Computational and Applied Mathematics*, **109**, 123
- Kley W., 1998, *A&A*, **338**, L37
- Kravtsov A. V., Klypin A. A., Khokhlov A. M., 1997, *ApJS*, **111**, 73
- Kritsuk A. G., et al., 2011, *ApJ*, **737**, 13
- Kuiper R., Klahr H., Dullemond C., Kley W., Henning T., 2010, *A&A*, **511**, A81
- Lodato G., Price D. J., 2010, *MNRAS*, **405**, 1212
- Masset F., 2000, *A&AS*, **141**, 165
- Masson J., Teyssier R., Mulet-Marquis C., Hennebelle P., Chabrier G., 2012, *ApJS*, **201**, 24
- Mendygral P. J., et al., 2017, *ApJS*, **228**, 23
- Mignone A., Bodo G., Massaglia S., Matsakos T., Tesileanu O., Zanni C., Ferrari A., 2007, *ApJS*, **170**, 228
- Nordlund A., 1982, *A&A*, **107**, 1
- Nordlund A., 1984, Iterative solution of radiative transfer problems with spherical symmetry using a single-ray approximation. Cambridge University Press, pp 211–233
- Nordlund Å., Galsgaard K., Stein R. F., 1994, in Rutten R. J., Schrijver C. J., eds, NATO Advanced Science Institutes (ASI) Series C Vol. 433, NATO Advanced Science Institutes (ASI) Series C. p. 471
- Nordlund Å., Haugbølle T., Küffmeier M., Padoan P., Vasileiades A., 2014, in Booth M., Matthews B. C., Graham J. R., eds, IAU Symposium Vol. 299, Exploring the Formation and Evolution of Planetary Systems. pp 131–135, doi:10.1017/S1743921313008107
- Padoan P., Zweibel E., Nordlund Å., 2000, *ApJ*, **540**, 332
- Paxton B., Bildsten L., Dotter A., Herwig F., Lesaffre P., Timmes F., 2010, MESA: Modules for Experiments in Stellar Astrophysics, Astrophysics Source Code Library (ascl:1010.083)
- Porth O., Xia C., Hendrix T., Moschou S. P., Keppens R., 2014, *ApJS*, **214**, 4
- Ramsey J. P., Dullemond C. P., 2015, *A&A*, **574**, A81
- Ramsey J. P., Clarke D. A., Men'shchikov A. B., 2012, *ApJS*, **199**, 13
- Shiokawa H., Cheng R. M., Noble S. C., Krolik J. H., 2017, preprint, (arXiv:1701.05610)
- Springel V., 2005, *MNRAS*, **364**, 1105
- Springel V., 2010, *MNRAS*, **401**, 791
- Stone J. M., Norman M. L., 1992, *ApJS*, **80**, 753
- Stone J. M., Mihalas D., Norman M. L., 1992, *ApJS*, **80**, 819
- Stone J. M., Gardiner T. A., Teuben P., Hawley J. F., Simon J. B., 2008, *ApJS*, **178**, 137
- Teyssier R., 2002, *A&A*, **385**, 337
- Ziegler U., 1998, *Computer Physics Communications*, **109**, 111
- de Val-Borro M., et al., 2006, *MNRAS*, **370**, 529
- van der Holst B., et al., 2011, *ApJS*, **194**, 23

This paper has been typeset from a  $\text{\TeX}/\text{\LaTeX}$  file prepared by the author.